Halide Exchange in Perovskites Enables Bromine/Iodine Hybrid Cathodes for Highly Durable Zinc Ion Batteries

Wang, Shixun; Wang, Yiqiao; Wei, Zhiquan; Zhu, Jiaxiong; Chen, Ze; Hong, Hu; Xiong, Qi; Zhang, Dechao; Li, Shimei; Wang, Shengnan; Huang, Yan; Zhi, Chunyi

Published in:
Advanced Materials

Published: 26/06/2024

Document Version:
Final Published version, also known as Publisher's PDF, Publisher's Final version or Version of Record

Published version (DOI):
10.1002/adma.202401924

Publication details:
Wang, S., Wang, Y., Wei, Z., Zhu, J., Chen, Z., Hong, H., Xiong, Q., Zhang, D., Li, S., Wang, S., Huang, Y., & Zhi, C. (2024). Halide Exchange in Perovskites Enables Bromine/Iodine Hybrid Cathodes for Highly Durable Zinc Ion Batteries. *Advanced Materials*, *36*(26), Article 2401924. https://doi.org/10.1002/adma.202401924

ADVANCED MATERIALS
www.advmat.de

Halide Exchange in Perovskites Enables Bromine/Iodine Hybrid Cathodes for Highly Durable Zinc Ion Batteries

*Shixun Wang, Yiqiao Wang, Zhiquan Wei, Jiaxiong Zhu, Ze Chen, Hu Hong, Qi Xiong, Dechao Zhang, Shimei Li, Shengnan Wang, Yan Huang, and Chunyi Zhi**

With the increasing need for reliable storage systems, the conversion-type chemistry typified by bromine cathodes attracts considerable attention due to sizeable theoretical capacity, cost efficiency, and high redox potential. However, the severe loss of active species during operation remains a problem, leading researchers to resort to concentrated halide-containing electrolytes. Here, profiting from the intrinsic halide exchange in perovskite lattices, a novel low-dimensional halide hybrid perovskite cathode, $TmdpPb_2[IBr]_6$, which serves not only as a halogen reservoir for reversible three-electron conversions but also as an effective halogen absorbent by surface Pb dangling bonds, C—H...Br hydrogen bonds, and Pb—I...Br halogen bonds, is proposed. As such, the Zn||$TmdpPb_2[IBr]_6$ battery delivers three remarkable discharge voltage plateaus at 1.21 V (I^0/I^-), 1.47 V (I^+/I^0), and 1.74 V (Br^0/Br^-) in a typical halide-free electrolyte; meanwhile, realizing a high capacity of over 336 mAh g^{-1} at 0.4 A g^{-1} and high capacity retentions of 88% and 92% after 1000 cycles at 1.2 A g^{-1} and 4000 cycles at 3.2 A g^{-1}, respectively, accompanied by a high coulombic efficiency of ≈99%. The work highlights the promising conversion-type cathodes based on metal–halide perovskite materials.

1. Introduction

Accompanied by the success of commercial intercalation-type lithium-ion batteries and the reaching of performance plateaus, the study on conversion-type cathodes returns revitalized due to high theoretical capacity, large-scale reserves, and remarkable security that satisfy the growing demand for large-scale grid energy storage.[1–5] Zinc anode attracts particular attention to adapt the conversion-type cathodes, given its high theoretical capacity of 819 mAh g^{-1}, low redox potential of −0.76 V (vs standard hydrogen electrode, SHE), and cost efficiency.[6–9] To date, various zinc-ion batteries based on conversion-type cathodes such as halogen materials (Cl_2, Br_2, I_2), chalcogenide materials (O_2, S, Se, Te), and metal–chalcogenide/halide derivates are proven applicable in a mild aqueous medium; while, behaving in the face of continuous loss/shuttle of active materials that causes fast capacity fading and undesired cycling performance.[10–12]

Still, the conversion-type cathodes are prized for the promising multiple electron reactions and high affordability, especially for the halogen-based cathodes that likewise favor a wide potential region including 0.53 V (vs SHE, I^0/I^-), 1.08 V (vs SHE, Br^0/Br^-), and 1.35 V (vs SHE, Cl^0/Cl^-).[13–16] To achieve stable chlorine chemistry, for example, one realizes it by using the saturated chloride electrolyte to compensate for the loss of chlorine elements on the cathode electrode, reckoning without the utilization ratio of chlorine.[16–18] The iodine cathode, on the other hand, suffers from relatively low redox potential and theoretical capacity (211 mAh g^{-1}).[19] Instead, the liquid bromine finds a balance between the highly reactive chlorine gas and solid but less positive iodine,[20] contributing to a high theoretical capacity of

S. Wang, Y. Wang, Z. Wei, J. Zhu, Z. Chen, H. Hong, S. Wang, Y. Huang, C. Zhi
Department of Materials Science and Engineering
City University of Hong Kong
83 Tat Chee Avenue, Hong Kong S.A.R. 999077, P. R. China
E-mail: cy.zhi@cityu.edu.hk

The ORCID identification number(s) for the author(s) of this article can be found under https://doi.org/10.1002/adma.202401924

DOI: 10.1002/adma.202401924

Q. Xiong, D. Zhang, S. Li, C. Zhi
Hong Kong Center for Cerebro-Cardiovascular Health Engineering (COCHE)
Shatin, NT, Hong Kong S.A.R. 999077, P. R. China

Y. Huang
Sauvage Laboratory for Smart Materials
School of Materials Science and Engineering
Harbin Institute of Technology
Shenzhen 518055, China

C. Zhi
Center for Advanced Nuclear Safety and Sustainable Development
City University of Hong Kong
Kowloon, Hong Kong S.A.R. 999077, P. R. China

334 mAh g^{-1} and a large energy density of 610 Wh kg^{-1}, as well as a high output voltage of 1.84 V when coupled with a zinc anode.[21] Nevertheless, the promising features of a bromine-based cathode occur in conjunction with the loss of bromine (due to its high vapor pressure of 184 mmHg at 25 °C) and a severe shuttle effect of Br_3^- anions during cycling, resulting in an irreversible capacity loss.[22]

In order to stabilize the bromine redox chemistry, researchers have primarily resorted to a concentrated aqueous metal–bromide electrolyte (up to 3.5 M) either alone or with a combination of organic bromide salts with branched alkanes such as tetrapropylammonium bromide (TPABr), methyl ethyl pyrrolidinium bromide (MEPBr), and 1-ethyl-1-methylpyrrolidinium bromide (MEPBr, which forms eutectic electrolyte with 2 M $ZnBr_2$ salts).[23–26] Those strategies are helpful to some extent; while, barely utilizing most bromine species concerning the overall capacity and the output voltage. Another option is introducing additional adsorbents in the cathode electrode to fix the oxidized Br^0 and intermediate Br_3^- and alleviate their undesired shuttle process.[27] For instance, Li et al. developed Ti_3C_2TX MXenes for a similar immobilization effect toward Br species; while, enduring an ill-defined discharging voltage plateau far below the theoretical upper limit (1.84 V vs Zn^{2+}/Zn) and a capacity retention of 81% after 2100 cycles at 2 A g^{-1}.[28] Apart from external fixtures, interactions between halogen species have proven helpful. Chen et al. used solid iodine monobromide (IBr) in the cathode to activate the redox reactions of both bromine and iodine with an ease shuttle effect and achieved 6000 cycles with a capacity retention of ≈82% at 2 A g^{-1}. However, the coulombic efficiency (CE) was somewhat above 95% and the I^+/I^0 redox pair was utterly absent even at a low current density of 0.2 A g^{-1}, let alone, the highly sloping voltage plateaus at ≈1.63 V and 1.28 V for the Br^0/Br^- and I^0/I^- redox pairs, respectively.

The motivation to enable the iodine/bromine redox chemistry reminds us of the high mobility of halide anions in perovskite materials (ABX_3, X = Cl, Br, I), of which intrinsic halide exchange can even occur in nanoscale scopes to offer possible fast kinetics of halogen species for improved battery performance.[29,30] Meanwhile, the perovskite surface is expected to deliver abundant active sites to confine bromine/iodine species inside the cathode part and facilitate the conversion reactions without bearing excess halide electrolytes.[31,32] Our prior studies confirmed the electrochemical reversibility of iodide anions in low-dimensional tin–iodide perovskites in Li-ion and Zn-ion batteries.[33,34] However, to our best knowledge, three-electron transfer of I/Br hybrid cathode in a halide-free electrolyte has not been achieved so far, together with an underutilized discharge plateau of the Br^0/Br^- redox pair.

Herein, we propose a low-dimensional 4,4′-trimethylenedi pyridinium lead iodide/bromide hybrid perovskite ($TmdpPb_2[IBr]_6$), as the cathode material, where the A-site aromatic diamine provides long-range intermolecular π-electron cloud and positively charged ammonium ions that form bulk materials with 1D Pb-X (X = Br, I) dimers. The remarkable and compact lattice arrangement ensures high structural stability with enough steric hindrance and surface energy to stabilize active halogen species for reliable three-electron transfer in a 2 M $ZnSO_4$ electrolyte. Therefore, reversible Br^0/Br^-, I^+/I^0, and I^0/I^- redox reactions ae successfully activated and manifested in three apparent discharge plateaus at 1.74, 1.46, and 1.22 V, contributing to an overall capacity of up to 336 mAh g^{-1}_{I+Br} and a high energy density of 441 Wh kg^{-1}_{I+Br}. The fabricated Zn ion batteries present a remarkable lifespan of over 1000 cycles at 1.2 A g^{-1} and 4000 cycles at 3.2 A g^{-1}.

2. Results and Discussion

2.1. Halide Exchange and Surface Adsorption

The halide exchange of perovskites refers to a reaction that external halide anions exchange with neighboring counterparts in the parent crystalline compound to realize a wholly or partially exchanged crystal lattice, as depicted in **Figure 1a**.[35] This feature has been widely accepted to finetune the bandgap and diffusion of carriers for optoelectronics ranging from perovskite nanocrystals to their bulk derivatives.[36,37] To overcome the fragile stability of conventional perovskites, low-dimensional metal-halide perovskite derivatives have attracted widespread consideration due to the adjustable long-chain organic component that forms potential barriers embedded inside the crystal lattice and endows the bulk materials with considerable stability.[38] The high structural tunability of low-dimensional perovskite cathode may take the opportunity to reach a compromise between localizations and electrochemical activities of elemental halogens.

We proposed a $TmdpPb_2I_6$ perovskite as the parent material to examine the halide exchange and the corresponding confinement effect for an adequate iodide/bromine hybrid perovskite cathode. As shown in Figure 1b, the aromatic cations electrostatically bound with lead iodide octahedral network in the form of cation–π stacking, resulting in the formation of a 1D $TmdpPb_2I_6$ perovskite with space group $C2/C$.[39] The 1D octahedral dimer was expected to experience a fast halide exchange when getting close to external bromide source and to release lattice iodide in the meanwhile, all of which favor the activation and stabilization of the Br^0/Br^-, I^+/I^0, and I^0/I^- redox pairs (Figure 1c). $TmdpPb_2I_6$ perovskite crystals were immersed into an aqueous Br_3^- solution and procured the accumulation of Br_3^- anions at the surface, according to the yellowish-brown color shown in Figure 1d, supported by its characteristic Raman signal in Figure S1, Supporting Information. UV–visible spectra presented in Figure 1e further witnessed the detailed exchange/adsorption process. The control solution had two prominent absorption peaks at 266 and 293 nm, corresponding to an even distribution of Br_3^- anions. The characteristic absorption peaks were significantly suppressed as the addition of $TmdpPb_2I_6$ perovskites, which caused the amassing of Br_3^- anions at the bottom of the cuvette and placed. The solution was stirred at varying periods to verify the species of surface adsorbates. One min after the agitation, the signal of I_3^- suddenly appeared at 278 nm, and 4 min later, the Br_2 molecules emerged at 460 nm. The observation revealed a combined process of halide exchange and adsorption of elemental halogens at the perovskite surface. For further details, the pristine $TmdpPb_2I_6$ and the obtained $TmdpPb_2[IBr]_6$ hybrid perovskite crystals were used for detailed characterizations. As shown in the Fourier transform infrared spectroscopy (FTIR) spectra in Figure 1f, the C—N

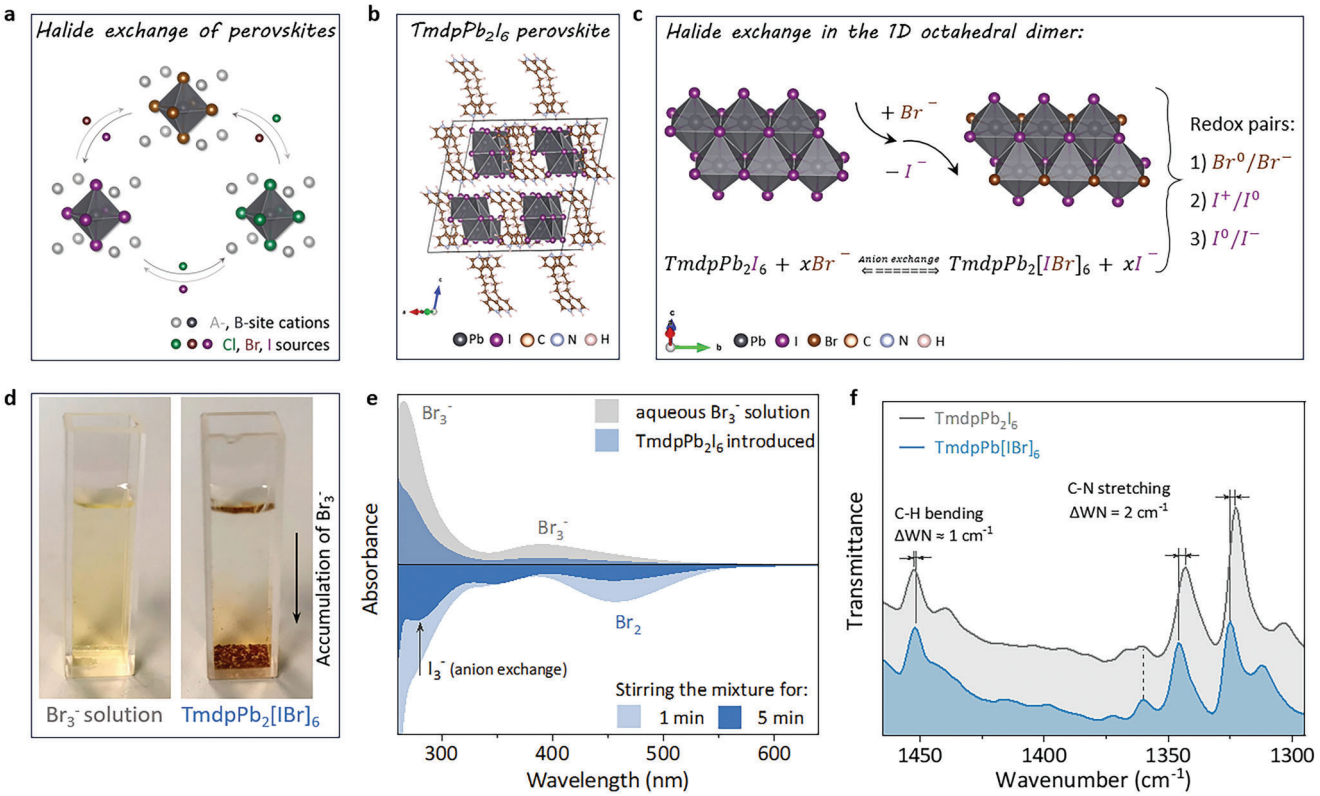

Figure 1. Halide exchange in $TmdpPb_2I_6$ perovskites characterized by molecular vibrations. a) Scheme of halide exchange in typical perovskites. b) Structural demonstration of $TmdpPb_2I_6$ perovskites and c) the corresponding halide exchange process. d) Photographs, e) UV–visible absorption spectra, and f) FTIR spectra of $TmdpPb_2I_6$ perovskite before and after halide exchange. The "WN" in (f) denotes the abbreviation of "wavenumber.".

stretching vibration of the A-site $Tmdp^{2+}$ cation underwent a blue shift of 2 cm^{-1} after halide exchange. It could be attributed to a shorter C—N bond length after incorporating bromide anions that reduced the degree of protonation of amines, as supported by the shorter N—H bond length of $TmdpPb_2Br_6$ perovskites shown in Figure S2, Supporting Information. After exposure to bromine sources, the slight red shift of the C—H bending vibration after halide exchange could be associated with surface-adsorbed bromide ions (in the form of C—H...Br hydrogen bonds).

Scanning electron microscopy (SEM) and SEM-mapping images in **Figure 2**a,b; Figure S3, Supporting Information exhibit a similar 1D feature of $TmdpPb_2I_6$ and $TmdpPb_2[IBr]_6$ perovskites, the latter of which specifically demonstrated the presence of both elemental iodine and bromine, verifying the favoring halide exchange. XRD patterns in Figure 2c explain a shrunk interplanar spacing of the (002) lattice plane from 11.9 to 11.2 Å after the anion exchange due to the size deviation between the two halogen anions, following the trend of lattice diffraction from $TmdpPb_2I_6$ to $TmdpPb_2Br_6$ (Figure S4, Supporting Information). Notably, the slight mismatch (<0.2°) between the experimental XRD of $TmdpPb_2I_6$ microcrystals and the simulated result (of its bulk crystals) could be attributed to the presence of defects and possible intercalation of iodide ions that expanded the lattice.[40,41] Energy dispersive spectroscopy (EDS) results in Figure 2d further convince the feasibility of halide exchange and successful incorporation of bromide anions, which increased from an atomic ratio of 1% to 55%. On the other hand, the perovskite surface where the lattice periodicity terminated would facilitate the adsorption of halogen elements. According to the density-functional theory (DFT) calculations,[42–44] both $TmdpPb_2I_6$ and $TmdpPb_2Br_6$ supplied enough chemical interaction forces toward oxidized halide elements, especially for trihalide anions that experienced threefold improved adsorption energy at perovskite surfaces, thereby being able to cope with their shuttle in the aqueous electrolyte (Figure 2e). Specifically, as presented in Figure 2f, $TmdpPb_2I_6$ could link with Br_3^- anions in the forms of Pb—I...Br halogen bonds, surface Pb dangling bonds, and C—H...Br hydrogen bonds, all of which contributed to large adsorption energy of −2.75 eV. In contrast, that for the polar water molecules, was −0.29 eV (Figure S5, Supporting Information).[41,45–46] The halogen and hydrogen bonds dominated the coordination with surface halogens (Br_2 and I_2) and I_3^- ions, respectively (Figures S6 and S7, Supporting Information). The IBr molecule, on the other hand, was linked by the two van der Waals forces, as shown in Figure S8, Supporting Information. $TmdpPb_2Br_6$, as illustrated in Figure 2g, provided a slightly weaker binding energy of −2.08 eV as the absence of surface Pb—I...Br halogen bonds, but good enough to uphold halogen confinement. Considering the multiple effective media at the lead–iodide perovskite surface and their relatively strong bonding forces, $TmdpPb_2I_6$ was adopted as the parent material for halide exchange to prepare $TmdpPb_2[IBr]_6$ hybrid perovskites for further study.

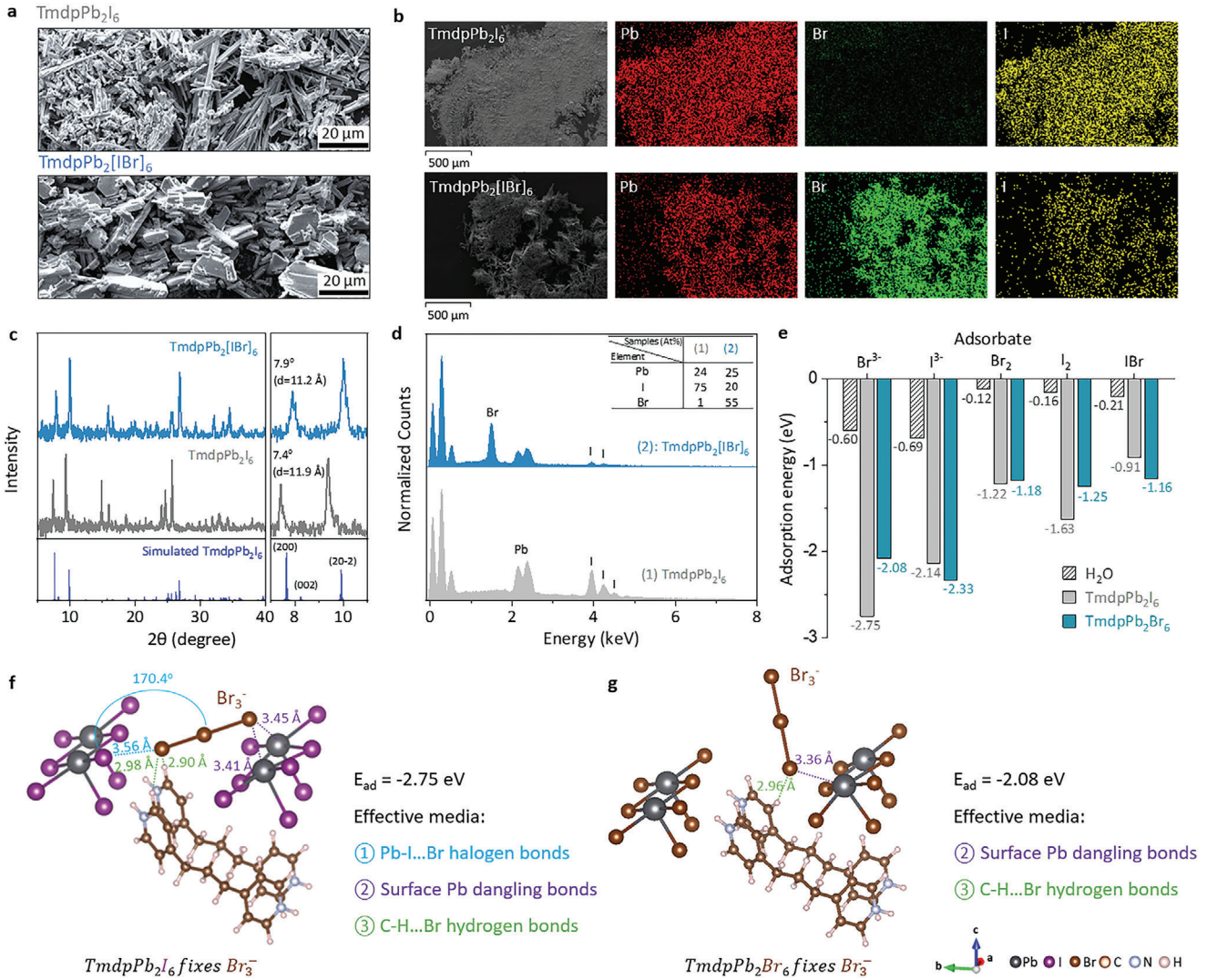

Figure 2. Characterizations of halide-exchanged perovskites and the corresponding DFT results. a) SEM, b) SEM-mapping images, c) XRD patterns, d) EDS spectra of $TmdpPb_2I_6$ perovskite before and after exposure to the aqueous Br_3^- solution, e) the surface adsorption energy of $TmdpPb_2I_6$ and $TmdpPb_2Br_6$ perovskites toward elemental Br/I and intermediate IBr compound, and f,g) detailed bond coordination with Br_3^- anions.

2.2. Halogen Redox of $TmdpPb_2[IBr]_6$

In order to validate the electrochemical activity of the proposed halide hybrid perovskite cathodes, Zn||2 M $ZnSO_4$||$TmdpPb_2[IBr]_6$ Swagelok cells were assembled for the cyclic voltammetry (CV) measurement. As shown in **Figure 3**a, the battery with perovskite cathodes sustained continuous CV scans from 0.1 to 10 mV s^{-1} with a reliable three-electron conversion including Br^0/Br^-, I^+/I^0, and I^0/I^-. The *b* value was calculated to evaluate the detailed oxidation–reduction process based on the equation $i = av^b$, where *i* and *v* corresponded to the response current and sweep rate.[15] Figure 3b shows anodic/cathodic peaks of the Zn||$TmdpPb_2[IBr]_6$ cells with *b* values sitting between 0.5 and 1, revealing a combined mode of semi-infinite diffusion-controlled faradaic process and surface-controlled capacitive process. We note that the cathodic reaction of bromine delivered a much lower *b* value of 0.61, which could be assigned to a more battery-type process of Br^0/Br^- than $I^+/I^0/I^-$ redox pairs. The quantitative contribution of the charge storage was further derived from the equation $i = k_1v + k_2v^{0.5}$, where k_1v was the capacitive part and $k_2v^{0.5}$ was the faradaic part.[47] The capacitive (surface-controlled) part of the Zn||$TmdpPb_2[IBr]_6$ cell accounted for 61.2% of all transferred charges when scanning at 1 mV s^{-1}, together with two redox pairs at 1.21/1.31 V for I^0/I^- and 1.44/1.57 V for I^+/I^0, as well as a dominant cathodic peak of bromines at 1.68 V (Figure 3c). The applied voltage range was set at ≈0.8–1.84 V to avoid the oxygen evolution reaction (OER, 1.98 V vs SHE) and electrolyte decomposition (Figure S9, Supporting Information).

The evolution of two mechanisms in the perovskite-based battery is summarized in Figure 3d as a function of scan rate. It reveals a fast-rising capacitive contribution of 34.1% at 0.1 mV s^{-1} to 87.7% at 10 mV s^{-1}. A continuous CV operation further evaluated the stability of the three redox pairs at 5 mV s^{-1} for 50

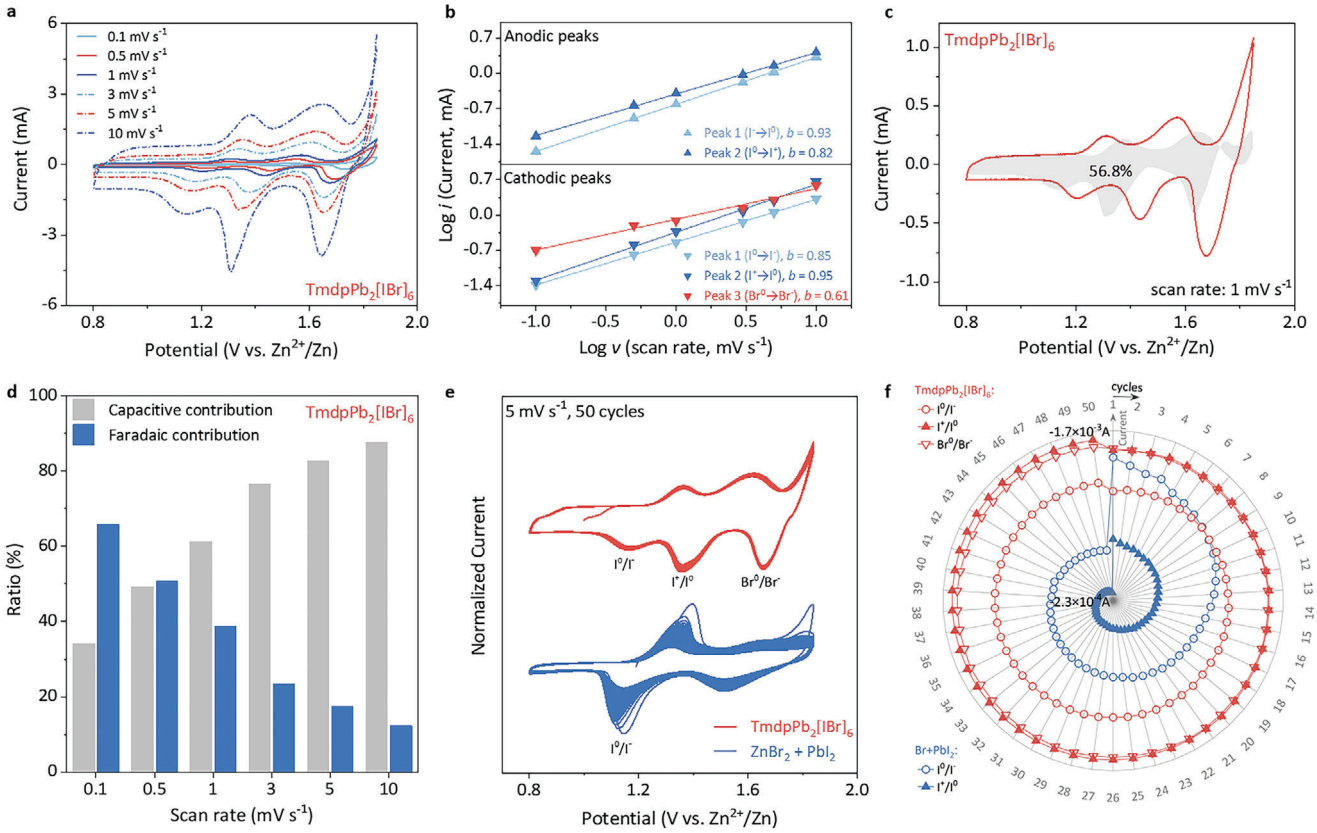

Figure 3. Redox properties and electrochemical characterizations of Zn||$TmdpPb_2[IBr]_6$ batteries. a) CV curves at various scan rates and b) the corresponding fitting plots between log(*i*) and log(*ν*) of the anodic and cathodic peaks. c) CV curves showing faradaic and capacitive contributions at 1 mV s^{-1} and d) at different scans as a summary diagram. e) Accumulation of CV curves scanned at 5 mV s^{-1} for 50 cycles and f) the corresponding current evolution of each cathodic peak.

cycles where the Zn||$TmdpPb_2[IBr]_6$ cell offered three consistent redox reactions (Figure 3e). Instead, a simple mixture of ZnBr and PbI_2 could only ignite two unstable I^+/I^0 and I^0/I^- redox pairs; the I^0/I^- possessed voltage polarization over 0.25 V while that for Zn||$TmdpPb_2[IBr]_6$ was less than 0.2 V. We note that the $TmdpPb_2[BrI]_6$ perovskite cathode, which used $TmdpPb_2Br_6$ as the parent material for halide exchange, also failed to activate the I^+/I^0 and Br^0/Br^- redox pairs, probably due to an unfavored lattice ordering on halide distribution (Figure S10, Supporting Information). $TmdpPb_2I_6$ cathode, on the other hand, only generated one reduction peak corresponding to the I^0/I^- redox pair (Figure S11, Supporting Information). Figure 3f further signifies the evolution of the response current at each anodic/cathodic peak. The cathodic current peak of the Zn||$TmdpPb_2[IBr]_6$ cells numerically formed a regular circle in the annular chart rather than that of the control sample, which suffered from a gradual degradation of the response currents. A similar trend was also observed on the anodic current peaks, as presented in Figure S12, Supporting Information.

2.3. Electrochemical Performances of the Zn||$TmdpPb_2[IBr]_6$

As for reliable halogen redox reactions on the perovskite cathodes, further studies were carried out on the electrochemical performance of Zn||$ZnSO_4$||$TmdpPb_2[IBr]_6$ batteries. The galvanostatic charge–discharge (GCD) curves recorded at a varying current from 0.4 to 3.2 A g^{-1} exhibited three typical charge/discharge plateaus (**Figure** 4a). They were attributed to the Br^0/Br^- (from 1.74 to 1.70 V), I^+/I^0 (1.47 to 1.43 V), and I^0/I^- (1.21 to 1.17 V) redox pairs, signifying the high stability and decent reversibility of the halogen redox reactions enabled by the perovskite cathodes. Moreover, the specific contributions of the discharge plateau to energy output were evaluated to be over 92% in the perovskite-based batteries, of which the Br^0/Br^- pair accounted for 53.3%; while, the two-electron process ($I^+/I^0/I^-$) contributed to 46.7% at 0.4 A g^{-1}. The rate capability performance was subsequently conducted within a wide current range of 0.4–3.2 A g^{-1}. As summarized in Figure 4b, the perovskite-based battery promoted a reversible energy density of 441 mWh g^{-1}_{I+Br} and capacity and 336 mAh g^{-1}_{I+Br} (over 100 mAh g^{-1} if normalized to the whole cathode electrode) at 0.4 A g^{-1}, approaching the theoretical limit of the above-coupled bromine/iodine redox pairs (374 mAh g^{-1}_{I+Br}). The capacity at 3.2 A g^{-1} was found to be 195 mAh g^{-1}_{I+Br} and increased to 332 mAh g^{-1}_{I+Br} again after the current reset.

Considering the liquid feature of oxidation productions, the study on the self-discharge properties of Zn||$TmdpPb_2[IBr]_6$ batteries was implemented to assess the effectiveness of immobilizing halogen elements. As shown in Figure 4c, the batteries experienced one cycle for battery activation; and subsequently,

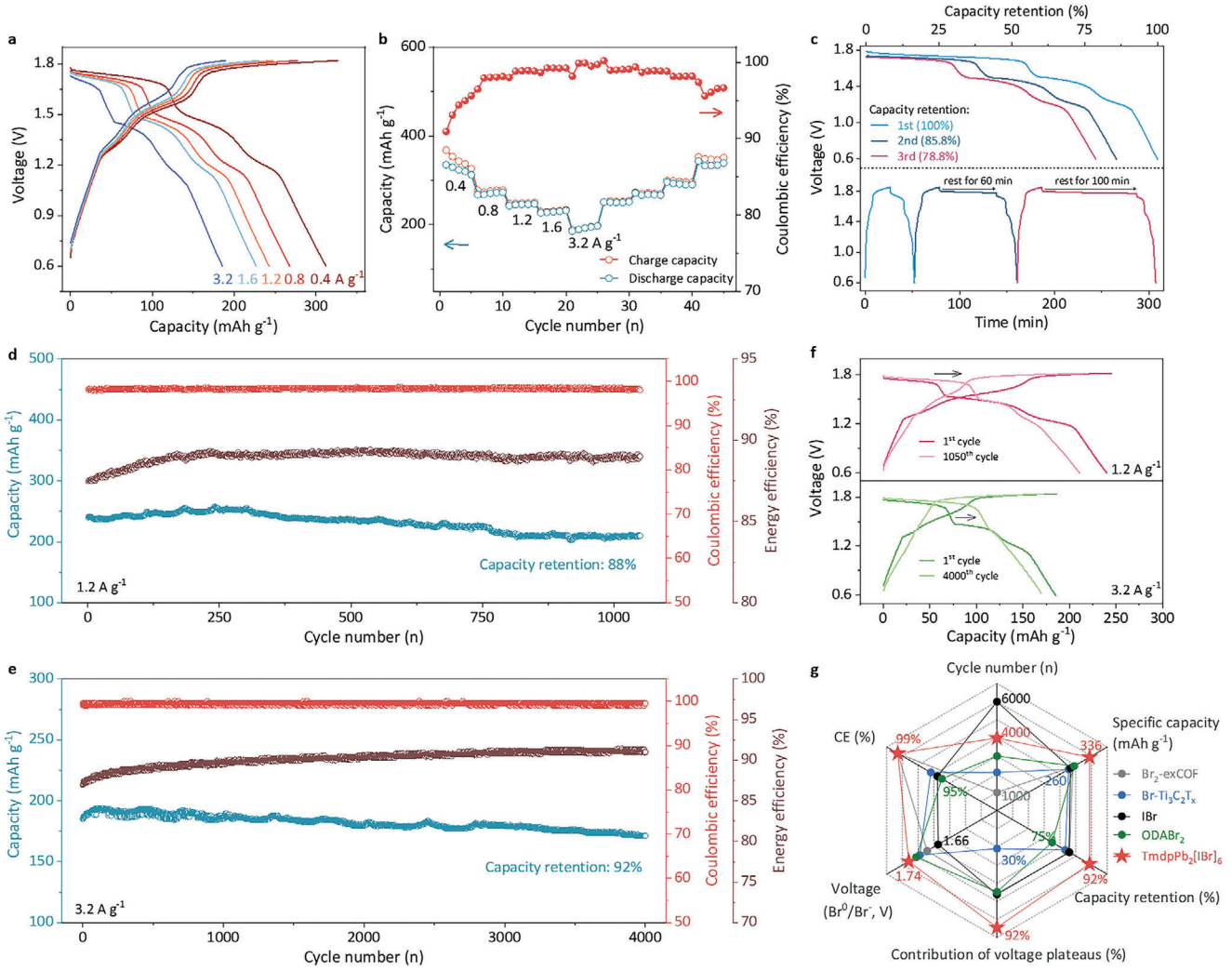

Figure 4. Electrochemical performance of Zn||$ZnSO_4$||$TmdpPb_2[IBr]_6$ batteries. a) GCD curves, b) rate capability, c) self-discharge spectra, and d) long-term cyclic performance at 1.2 A g^{-1} and e) 3.2 A g^{-1}. f) GCD curves at different cycles and g) figure of merits comparing with metal–iodine/bromine batteries reported in the literature.

charged to 1.82 V and stood for 60 min before discharging, followed by a third charging/discharging process. Compared with the 1st discharging capacity, a considerable capacity retention of 85.8% was achieved after an hour of standing and maintained at 78.8% even after a longer resting time of 100 min on account of well-suppressed trihalide anions shuttling. Once extending the resting time to over 14 h, a champion capacity retention of 77.9% was achieved, though the Br^0/Br^- and I^+/I^- redox reactions overlapped (Figure S13, Supporting Information). The findings exhibited the favorable potential of the low-dimensional perovskites cathode materials for metal–iodide/bromide batteries.

The durability of the perovskite-based batteries was further appraised by the long-term cycling measurement as presented in Figure 4d,e. The Zn||$TmdpPb_2[IBr]_6$ batteries could maintain a high capacity retention of 88% after operating 1000 cycles at a low current density of 1.2 A g^{-1} and went through a slight fall in the capacity of 8% after 4000 cycles at 3.2 A g^{-1}, during which a high CE of ≈99% was achieved, substantiating the high reliability of the designed perovskite cathodes. It was noted that the energy efficiency of the batteries increased from 87% to 89% at 1.2 A g^{-1} and from 87% to 91% at 3.2 A g^{-1}, which could be attributed to a continuous nanomerization of perovskite crystals that offered an increasing number of surface site for bromide adsorption. Likewise, improved electrolyte infiltration enabled efficient halogen redox reactions over time to reach a rising energy efficiency, supported by the reduced charge transfer resistance (Figure S14, Supporting Information). Specifically, as shown in Figure 4f, the Br^0/Br^- voltage plateaus continuously expanded during the cycling process, regardless of the applied current density. In comparison, the voltage contribution from the $I^+/I^0/I^-$ redox pairs was getting less distinct, arising from the stronger confinement toward bromine elements at the perovskite surface, as evidenced by the DFT calculations and ultra-violet absorption spectra (Figure S15, Supporting Information).[48] The phenomenon stresses the significance of the lattice ordering of perovskite structures for conversion-type cathodes. Notably, after

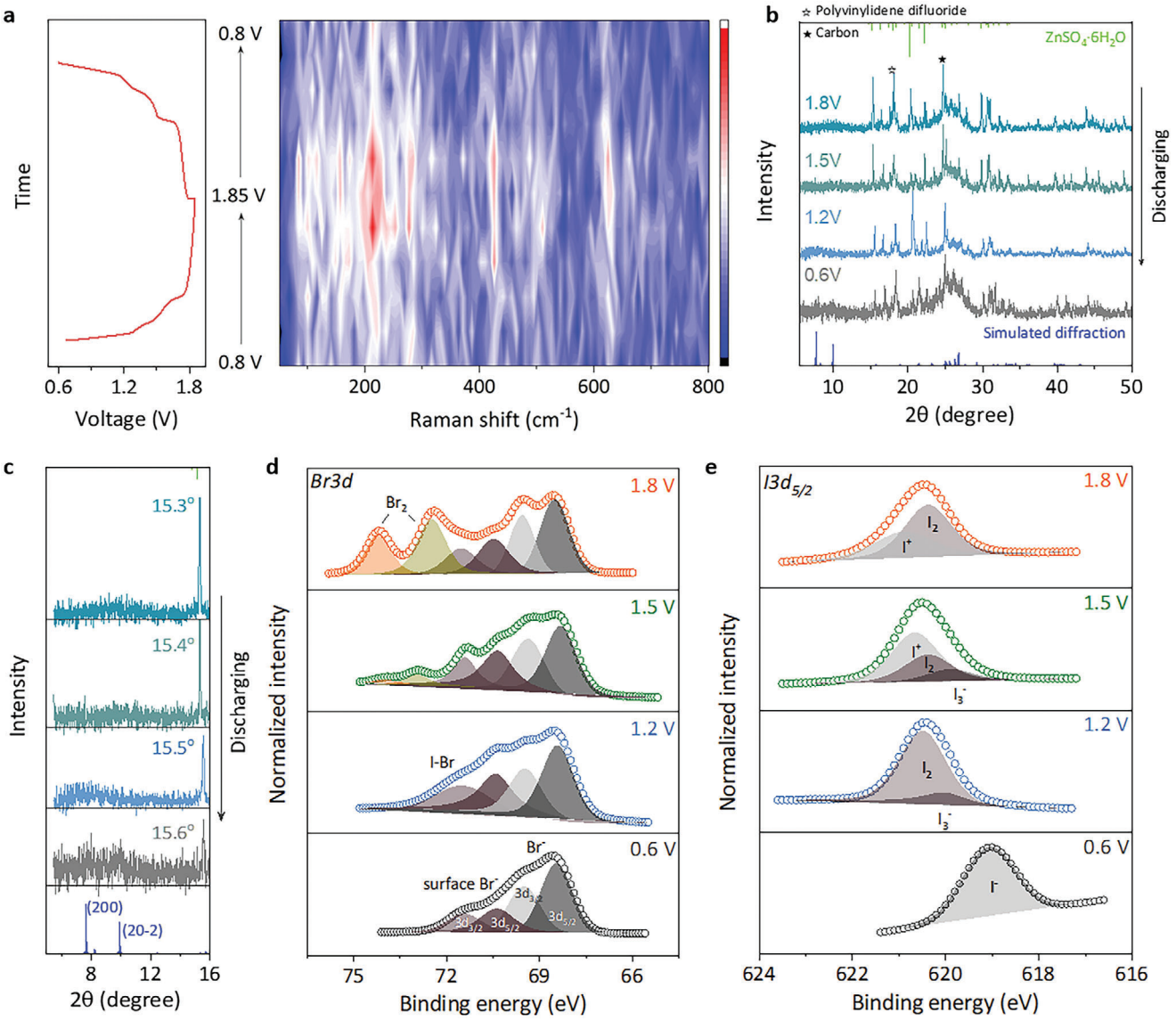

Figure 5. Redox chemistry and structural characterizations of Zn||TmdpPb$_2$[IBr]$_6$ batteries. a) Charge and discharge curves and corresponding 2D in situ Raman spectral mapping during the charging and discharging processes. b) XRD patterns of the perovskite cathode recorded at different discharging states and c) the corresponding expanded area. XPS spectra of d) Br3d and e) I3d$_{5/2}$ core levels.

long-term cycling, we found those batteries could fail by presenting a single $I^+/I^0/I^-$ redox reaction and a fast capacity fading, which probably arose from the complete decomposition or loss of perovskite lattices in the cathode electrode. (Figure S16, Supporting Information)

Critical indicators of most reported metal–iodine/bromine batteries with the use of aqueous halide-free electrolytes are summarized for comparison in Figure 4g.[15,27,28,49] Notably, bromine featured a high theoretical voltage of 1.84 V (vs Zn^{2+}/Zn^0). However, the reported Zn ion batteries with Br cathode typically delivered a voltage output below 1.7 V. In contrast, for the TmdpPb$_2$[IBr]$_6$, a voltage plateau of 1.74 V was achieved, with only a 0.05 V voltage loss at the end of the discharging process compared to the counterparts (Figure S17, Supporting Information). Moreover, the Zn||ZnSO$_4$||TmdpPb$_2$[IBr]$_6$ batteries outperformed all the counterparts with respect to capacity retention (92%, 4000 cycles), large specific capacity (336 mAh g^{-1}), and remarkable contribution of voltage plateaus (92%) on the strength of the efficient faradaic conversion in perovskite cathodes.

2.4. Redox Chemistry at Different Discharging States

To further reveal the reaction mechanism of the TmdpPb$_2$[IBr]$_6$ perovskite cathode, in situ Raman characterization during one battery cycle was performed as shown in **Figure 5a**. With the increase of the charging/discharging voltage, the vibration from I_3^- (112 cm^{-1}) and Br_3^- (157 cm^{-1}) gradually appeared with apparent I–Br interactions on account of intermediate IBr and IBr_2^-, as well as mild Br—Br bond vibrations at ≈310 cm^{-2},[25,26,50,51]

all of which proved the reversible three-electron conversion from Br^0/Br^- and $I^+/I^0/I^-$ redox pairs.[52] The charged perovskite cathodes were also taken to XRD measurements to examine the lattice change despite the conversion-type mechanism, as shown in Figure 5b. We noted a continuous lattice shrinkage from 15.3° at 1.8 V to 15.6° at 0.6 V, which refers to the (110) lattice plane of the $ZnSO_4{\cdot}6H_2O$ crystal. The observation suggests the existence of a secondary phase that occupied lattice voids and resulted in lattice dilatation during the volatilization and crystallization of electrolyte drops (Figure 5c). With a view to the strong bond strength and consistent bulges at lower diffraction degrees (Figures S18 and S19, Supporting Information), the perovskite crystal could probably reach the nanoscale or even form into an amorphous phase after cycling instead of fully decomposing into charged ions, attested by the battery failure from a simple halide mixture, as discussed in Figure 3e. The halogen redox chemistry of the perovskite cathode was further validated by the XPS measurements. The Br3d core level spectra in Figure 5d witnessed the whole oxidation process of bromide anions that were charged to IBr_2^-, represented by an emerging tail over 72 eV at 1.5 V, and turned to bromine molecules at 1.8 V, which possessed dual peaks at 72.46 and 74.21 eV.[53] Similarly, the binding energy of iodide anion shown in Figure 5e experienced a change from 619.08 eV (I^-, 0.6 V) to 620.5 eV (I_2, 1.2 V), 620.62 eV (I^+ in IBr, 1.5 V), and 620.88 eV (I^+ in IBr_2^-, 1.8 V). Notably, we infer the extra signal from iodine at 1.8 V from the disproportionation of metastable I^+ cations and oxidation of I^- anions by oxygen during the storage period before the XPS test, with the consideration of invisible intermediate triiodide anions.

3. Conclusion

In summary, we exhibited highly durable zinc-halogen batteries by harnessing the anion exchange properties for an iodide/bromide hybrid low-dimensional perovskite cathode—$TmdpPb_2[IBr]_6$. They were found to be an effective absorbent depending on Pb–I…Br halogen bonds, surface Pb dangling bonds, and C—H…Br hydrogen bonds that prevented the active halogen species from the undesired but general shuttle process. The proposed battery configuration successfully enabled a reliable I/Br three-electron transfer in a halide-free aqueous electrolyte (2 M $ZnSO_4$). As a result, the Zn||$TmdpPb_2[IBr]_6$ battery demonstrated a high capacity of over 336 mAh g^{-1}_{I+Br} at 0.4 A g^{-1}, together with three remarkable voltage plateaus at 1.74, 1.47, and 1.21 V, corresponding to the Br^0/Br^-, I^+/I^0, and I^0/I^- redox pairs, respectively. The long-term cycling performance further suggested the effectiveness of the perovskite cathodes, where high capacity retentions of 88% and 92% were realized after 1000 and 4000 cycles at 1.2 and 3.2 A g^{-1}, respectively, accompanied by a high CE of ≈99%.

Supporting Information

Supporting Information is available from the Wiley Online Library or from the author.

Acknowledgements

The research described in this paper was supported by the National Key Research and Development Program of China under Project 2019YFA0705104, the GRFs under Project CityU 11214023 and grants from the Research Grants Council of the Hong Kong Special Administrative Region China (Project No. R5019-22, Project No. CityU PDFS2122-1S05, and Project No. CityU 11214023). This work was also supported by the Talent Recruitment Project of Guangdong Province (No. 2019QN01C883), the Shenzhen Science and Technology Innovation Project (JCYJ20220818102402004), and the HIT-CityU Joint Laboratory on Zinc-based Batteries.

Conflict of Interest

The authors declare no conflict of interest.

Author Contributions

Shi.W. and C.Z. designed the study. C.Z. supervised the experiments. Shi.W., Y.W., Z.W., J.Z., Z.C., H.H., Q.X., D.Z., S.L., She.W., and Y.H. conducted structural, electrochemical, and spectroscopic characterizations and analyzed the data. Shi.W. performed the theoretical calculations. All authors discussed the results and commented on the manuscript.

Data Availability Statement

The data that support the findings of this study are available from the corresponding author upon reasonable request.

Keywords

halogen cathode, low-dimensional perovskites, metal–halogen batteries, zinc ion batteries

Received: February 5, 2024
Revised: March 22, 2024
Published online: April 15, 2024

[1] S. H. Yu, X. Feng, N. Zhang, J. Seok, H. D. Abruna, *Acc. Chem. Res.* **2018**, *51*, 273.
[2] H. Wang, S. Chen, C. Fu, Y. Ding, G. Liu, Y. Cao, Z. Chen, *ACS Mater. Lett.* **2021**, *3*, 956.
[3] X. Li, Y. Wang, J. Lu, S. Li, P. Li, Z. Huang, G. Liang, H. He, C. Zhi, *Angew. Chem., Int. Ed.* **2023**, *62*, 202310168.
[4] Z. Chen, Y. Hou, Y. Wang, Z. Wei, A. Chen, P. Li, Z. Huang, N. Li, C. Zhi, *Adv. Mater.* **2023**, *36*, 2309330.
[5] R. Wang, M. Yao, M. Yang, J. Zhu, J. Chen, Z. Niu, *Proc. Natl. Acad. Sci. U. S. A.* **2023**, *120*, 2221980120.
[6] M. Zhu, J. Hu, Q. Lu, H. Dong, D. D. Karnaushenko, C. Becker, D. Karnaushenko, Y. Li, H. Tang, Z. Qu, J. Ge, O. G. Schmidt, *Adv. Mater.* **2021**, *33*, 2007497.
[7] Y. Wang, B. Liang, J. Zhu, G. Li, Q. Li, R. Ye, J. Fan, C. Zhi, *Angew. Chem., Int. Ed.* **2023**, *62*, 202302583.
[8] Y. Wang, T. Wang, S. Bu, J. Zhu, Y. Wang, R. Zhang, H. Hong, W. Zhang, J. Fan, C. Zhi, *Nat. Commun.* **2023**, *14*, 1828.
[9] J. Zhou, Y. Xiong, M. Sun, Z. Xu, Y. Wang, P. Lu, F. Liu, F. Hao, T. Feng, Y. Ma, J. Yin, C. Ye, B. Chen, S. Xi, Y. Zhu, B. Huang, Z. Fan, *Proc. Natl. Acad. Sci. U. S. A.* **2023**, *120*, 2311149120.
[10] W. Li, D. Wang, *Adv. Mater.* **2023**, 2304983.
[11] Z. Chen, S. Wang, Z. Wei, Y. Wang, Z. Wu, Y. Hou, J. Zhu, Y. Wang, G. Liang, Z. Huang, A. Chen, D. Wang, C. Zhi, *J. Am. Chem. Soc.* **2023**, *145*, 20521.

[12] Z. Chen, Q. Yang, F. Mo, N. Li, G. Liang, X. Li, Z. Huang, D. Wang, W. Huang, J. Fan, C. Zhi, *Adv. Mater.* **2020**, *32*, 2001469.
[13] D. Lin, Y. Li, *Adv. Mater.* **2022**, *34*, 2108856.
[14] P. Li, C. Li, X. Guo, X. Li, C. Zhi, *Bull. Chem. Soc. Jpn.* **2021**, *94*, 2036.
[15] X. Li, S. Wang, T. Wang, Z. Duan, Z. Huang, G. Liang, J. Fan, C. Yang, A. L. Rogach, C. Zhi, *Nano Energy* **2022**, *98*, 107278.
[16] X. Zhang, H. Wei, S. Li, B. Ren, J. Jiang, G. Qu, H. Lv, G. Liang, G. Chen, C. Zhi, H. Li, Z. Liu, *Nat. Commun.* **2023**, *14*, 6738.
[17] G. Liang, B. Liang, A. Chen, J. Zhu, Q. Li, Z. Huang, X. Li, Y. Wang, X. Wang, B. Xiong, X. Jin, S. Bai, J. Fan, C. Zhi, *Nat. Commun.* **2023**, *14*, 1856.
[18] S. Geng, X. Zhao, Q. Xu, B. Yuan, Y. Wang, M. Liao, L. Ye, S. Wang, Z. Ouyang, L. Wu, Y. Wang, C. Ma, X. Zhao, H. Sun, *Nat. Commun.* **2024**, *15*, 944.
[19] T. Zhang, Y. Tang, S. Guo, X. Cao, A. Pan, G. Fang, J. Zhou, S. Liang, *Energy Environ. Sci.* **2020**, *13*, 4625.
[20] P. Li, X. Li, Y. Guo, A. Chen, R. Zhang, Y. Hou, Q. Xiong, Y. Wang, Z. Chen, J. Zhu, M. Zhu, C. Zhi, *Chem* **2023**, *10*, 352.
[21] H. Ma, X. Wang, C. Wang, H. Zhang, X. Ma, W. Deng, R. Chen, T. Cao, Y. Chai, Y. He, W. Ji, R. Li, J. Chen, J. Ji, W. Rao, M. Xue, *Small* **2022**, *19*, 2205071.
[22] S. Biswas, A. Senju, R. Mohr, T. Hodson, N. Karthikeyan, K. W. Knehr, A. G. Hsieh, X. Yang, B. E. Koel, D. A. Steingart, *Energy Environ. Sci.* **2017**, *10*, 114.
[23] L. Gao, Z. Li, Y. Zou, S. Yin, P. Peng, Y. Shao, X. Liang, *iScience* **2020**, *23*, 101348.
[24] J. H. Lee, Y. Byun, G. H. Jeong, C. Choi, J. Kwen, R. Kim, I. H. Kim, S. O. Kim, H. T. Kim, *Adv. Mater.* **2019**, *31*, 1904524.
[25] S. Lv, T. Fang, Z. Ding, Y. Wang, H. Jiang, C. Wei, D. Zhou, X. Tang, X. Liu, *ACS Nano* **2022**, *16*, 20389.
[26] J. Heo, K. Shin, H. T. Kim, *Adv. Sci.* **2022**, *9*, 2204908.
[27] Y. Zhang, C. Wei, M.-X. Wu, Y. Wang, H. Jiang, G. Zhou, X. Tang, X. Liu, *Chem. Eng. J.* **2023**, *451*, 138915.
[28] X. Li, N. Li, Z. Huang, Z. Chen, Y. Zhao, G. Liang, Q. Yang, M. Li, Q. Huang, B. Dong, J. Fan, C. Zhi, *ACS Nano* **2021**, *15*, 1718.
[29] N. Livakas, S. Toso, Y. P. Ivanov, T. Das, S. Chakraborty, G. Divitini, L. Manna, *J. Am. Chem. Soc.* **2023**, *145*, 20442.
[30] C. Bi, S. Wang, W. Wen, J. Yuan, G. Cao, J. Tian, *J. Phys. Chem. C* **2018**, *122*, 5151.
[31] S. Wang, X. Shen, Y. Zhang, X. Zhuang, D. Xue, X. Zhang, J. Wu, J. Zhu, Z. Shi, S. V. Kershaw, W. W. Yu, A. L. Rogach, *Small* **2019**, *15*, 1901828.
[32] S. Wang, Y. Wang, Y. Zhang, X. Zhang, X. Shen, X. Zhuang, P. Lu, W. W. Yu, S. V. Kershaw, A. L. Rogach, *J. Phys. Chem. Lett.* **2019**, *10*, 90.
[33] S. Wang, Z. Huang, B. Tang, X. Li, X. Zhao, Z. Chen, C. Zhi, A. L. Rogach, *Adv. Energy Mater.* **2023**, *13*, 2300922.
[34] X. Li, S. Wang, D. Zhang, P. Li, Z. Chen, A. Chen, Z. Huang, G. Liang, A. L. Rogach, C. Zhi, *Adv. Mater.* **2023**, *36*, 2304557.
[35] H. Jiang, S. Cui, Y. Chen, H. Zhong, *Nano Select* **2021**, *2*, 2040.
[36] G. Nedelcu, L. Protesescu, S. Yakunin, M. I. Bodnarchuk, M. J. Grotevent, M. V. Kovalenko, *Nano Lett.* **2015**, *15*, 5635.
[37] X. Guan, Z. Lei, X. Yu, C. H. Lin, J. K. Huang, C. Y. Huang, L. Hu, F. Li, A. Vinu, J. Yi, T. Wu, *Small* **2022**, *18*, 2203311.
[38] M. I. Saidaminov, O. F. Mohammed, O. M. Bakr, *ACS Energy Lett.* **2017**, *2*, 889.
[39] T. Sheikh, S. Maqbool, P. Mandal, A. Nag, *Angew. Chem., Int. Ed.* **2021**, *60*, 18265.
[40] T. Sheikh, V. Nawale, N. Pathoor, C. Phadnis, A. Chowdhury, A. Nag, *Angew. Chem., Int. Ed.* **2020**, *59*, 11653.
[41] S. Wang, C. Bi, A. Portniagin, J. Yuan, J. Ning, X. Xiao, X. Zhang, Y. Y. Li, S. V. Kershaw, J. Tian, A. L. Rogach, *ACS Energy Lett.* **2020**, *5*, 2401.
[42] S. Wang, R. Shi, B. Tang, Y. Xiong, A. Portniagin, X. Zhao, S. V. Kershaw, R. Long, A. L. Rogach, *Nanoscale* **2022**, *14*, 15691.
[43] S.-H. Wei, S. B. Zhang, *Phys. Rev. B: Condens. Matter Mater. Phys.* **2002**, *66*, 155211.
[44] J. P. Perdew, K. Burke, M. Ernzerhof, *Phys. Rev. Lett.* **1996**, *77*, 3865.
[45] S. Wang, S. V. Kershaw, A. L. Rogach, *Chem. Mater.* **2021**, *33*, 5413.
[46] S. Wang, J. Popović, S. Burazer, A. Portniagin, F. Liu, K. H. Low, Z. Duan, Y. Li, Y. Xiong, Y. Zhu, S. V. Kershaw, A. B. Djurišić, A. L. Rogach, *Adv. Funct. Mater.* **2021**, *31*, 2102182.
[47] J. Liu, J. Wang, C. Xu, H. Jiang, C. Li, L. Zhang, J. Lin, Z. X. Shen, *Adv. Sci.* **2018**, *5*, 1700322.
[48] D. N. Makhayeva, G. S. Irmukhametova, V. V. Khutoryanskiy, *Rev. J. Chem.* **2020**, *10*, 40.
[49] S. Chen, Y. Ying, S. Wang, L. Ma, H. Huang, X. Wang, X. Jin, S. Bai, C. Zhi, *Angew. Chem., Int. Ed.* **2023**, *62*, 202301467.
[50] H. Liu, C. Y. Chen, H. Yang, Y. Wang, L. Zou, Y. S. Wei, J. Jiang, J. Guo, W. Shi, Q. Xu, P. Cheng, *Adv. Mater.* **2020**, *32*, 2004553.
[51] A. A. Bernussi, G. M. Gualberto, *J. Raman Spectrosc.* **2005**, *18*, 93.
[52] E. T. Branigan, N. Halberstadt, V. A. Apkarian, *J. Chem. Phys.* **2011**, *134*, 174503.
[53] A. Hultqvist, T. J. Jacobsson, S. Svanstrom, M. Edoff, U. B. Cappel, H. Rensmo, E. M. J. Johansson, G. Boschloo, T. Torndahl, *ACS Appl. Energy Mater.* **2021**, *4*, 510.